GLOBAL FRICTION OF
UNIFORM VS. HETEROGENEOUS SANDPAPER ROUGHNESS

Lars H. von Deyn, Alexander Stroh, Davide Gatti and Bettina Frohnapfel
Institute of Fluid Mechanics
Karlsruhe Institute of Technology
76131 Karlsruhe, Germany
von-deyn@kit.edu

Abstract

Skin-friction measurements of streamwise aligned sandpaper strips are presented in Nikuradse-type diagrams obtained in a dedicated experimental facility. These novel results shed light onto the global friction drag of heterogeneous rough surfaces. They indicate the drag-increasing presence of secondary motions known to exist over spanwise heterogeneous roughness. The Reynolds number dependency of the skin-friction coefficient appears to be a superposition of the smooth wall and homogeneous rough wall behavior. The results suggest that the present heterogeneous rough surface does not reach a fully rough behavior in which the friction coefficient becomes independent of Reynolds number.

1 Introduction

Predicting the global friction drag of rough surfaces poses a challenge which is subject of ongoing research. Especially heterogeneous roughness effects are not yet included in existing predictive frameworks (Chung *et al.*, 2021). Nevertheless, inhomogeneous roughness is a key feature of many environmental and engineering surfaces (Colombini & Parker, 1995; Bons *et al.*, 2001). The present work aims at providing reliable friction measurements for spanwise heterogeneous roughness over a broad Reynolds number range and thus novel data for possible future engineering correlations.

Surfaces with inhomogeneity normal to the mean flow direction are known to produce large-scale secondary motions of Prandtl's second kind that can alter the drag and heat transfer properties of a turbulent boundary layer (see e.g. Stroh *et al.*, 2019) and are thus important to be considered in predictive frameworks. From literature, it is known that protruding and δ-spaced ridges (δ is the characteristic outer length scale, here mean half-channel height) produce strong secondary currents (Vanderwel & Ganapathisubramani, 2015; Medjnoun *et al.*, 2020). This simplified configuration is often termed *ridge-type* roughness. Additionally, spanwise alternating strips of high and low wall friction (such that the roughness elevation can be neglected) termed *strip-type* roughness are often investigated due to its easy accessibility especially in numerical simulations (Chung *et al.*, 2018).

Medjnoun *et al.* (2020) investigated the friction behavior of smooth protruding ridges of various shapes
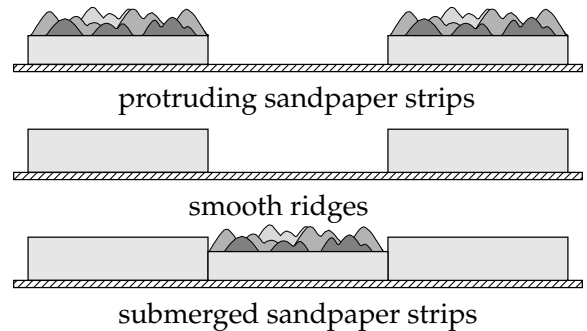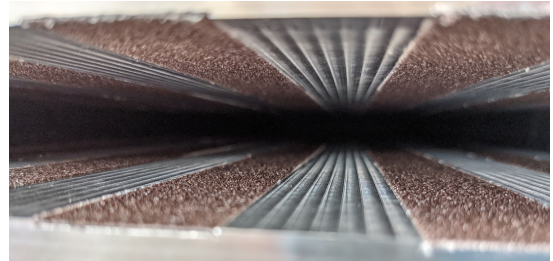

Figure 1: Experimental setup. bottom: schematic representation of measured surface configurations. Top: Photograph of $s \approx 4\delta_{\text{avg}}$ spaced submerged roughness strips built in the wind tunnel test section (view from tunnel exit)

and reported an upward shift of the smooth reference curve dependent on the structures shape, i.e. magnitude of the secondary flows. In accordance with these findings, we choose two spanwise wavelengths $s \approx 2\delta_{\text{avg}}$ $s \approx 4\delta_{\text{avg}}$ spanwise spacing and add sandpaper roughness on top of the smooth ridges as a step closer to "real world inhomogeneous roughness". δ_{avg} denotes the geometrically averaged channel half-height throughout the manuscript. In addition to these protruding roughness strips, we also investigate streamwise strips of submerged sandpaper roughness which are similar to the configuration studied by Wangsawijaya *et al.* (2020). The results are presented in Nikuradse-type and roughness function diagrams in comparison with smooth and homogeneous rough references.

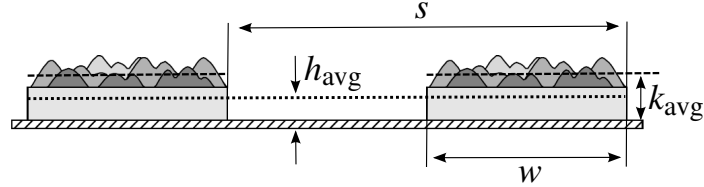| ID	s [mm]	k_{avg} [mm]	h_{avg} [mm]	$\frac{s}{\delta_{avg}}$	$\frac{k_{avg}}{\delta_{avg}}$	$\frac{h_{avg}}{\delta_{avg}}$	$\frac{s}{w}$	$\frac{k_{avg}}{k_s}$
smooth	-	-	-	-	-	-	-	-
homogen_rgh	-	0.67	0.67	-	0.055	0.055	-	1.169
protruding_rgh_2δ	25	0.67	0.335	2.038	0.054	0.027	1	0.568
protruding_rgh_4δ	50	.67	0.335	4.076	0.054	0.027	1	0.429
ridge_2δ	25	0.67	0.335	1.926	0.053	0.026	1	-
ridge_4δ	50	0.67	0.335	3.852	0.053	0.026	1	-
submerged_rgh_2δ	25	0.67	0	1.976	0.054	0	1	0.505
submerged_rgh_4δ	50	0.67	0	3.952	0.054	0	1	0.429

Table 1: Overview of investigated geometries. δ_{avg} denotes the average half-channel height defined with h_{avg}.
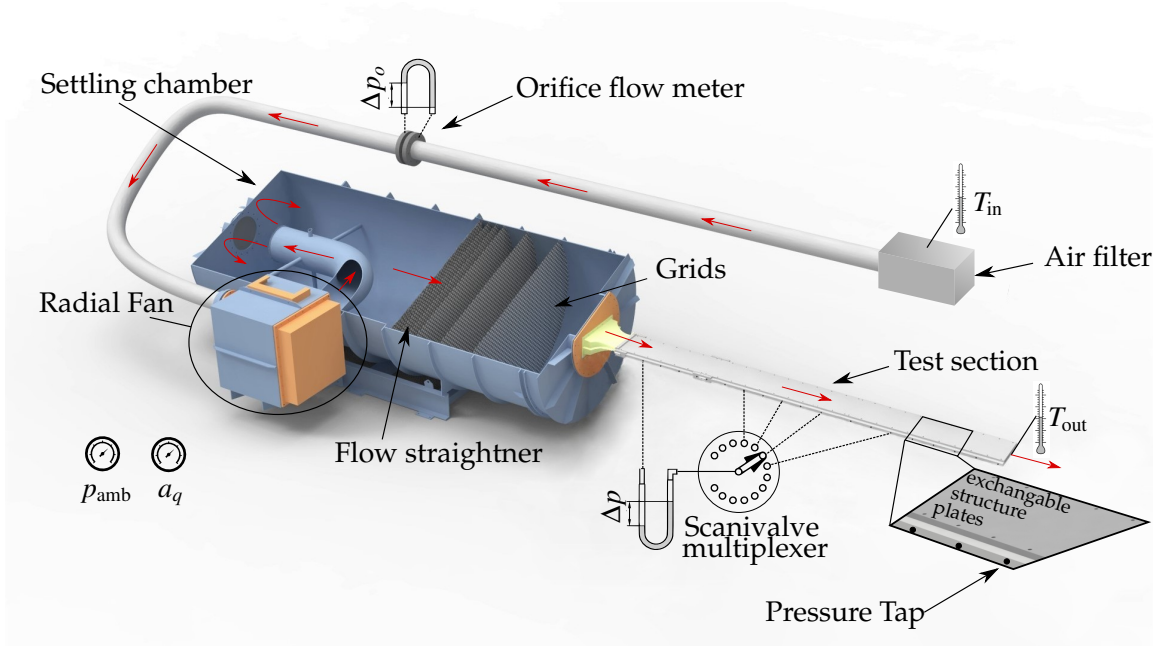

Figure 2: Schematic of the utilized wind tunnel including measurement instrumentation.

2 Investigated Geometries

Measurements are carried out in the three different configurations depicted in figure 1. We consider streamwise aligned spanwise alternating strips of smooth aluminium and P-60 grit sandpaper at two different spanwise wavelengths $s/\delta_{avg} \approx 2$ and $s/\delta_{avg} \approx 4$. The protruding sandpaper roughness configuration denoted protruding_rgh_xδ, where x represents the approximated wave length s/δ_{avg}, was manufactured by gluing sandpaper strips on a smooth aluminium plate, resulting in spanwise alternating smooth and protruding sandpaper strips. Thus, the domain-averaged roughness height is $h_{avg} > 0$ (see figure below table 1 for definitions).

Additionally, notches of the averaged sandpaper height's depth were milled in aluminium plates with a high precision milling machine. This configuration was measured in the wind tunnel in order to quantify the effect of smooth protruding ridges (termed ridge_xδ in table 1) on friction drag without sandpaper roughness. Afterwards, sandpaper strips were glued
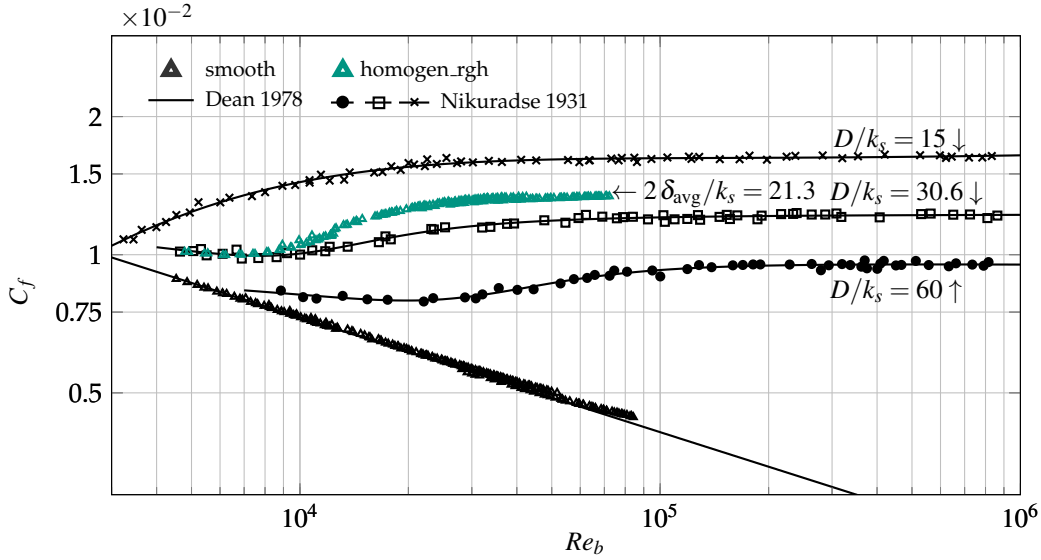
Figure 3: C_f vs. Re_b of smooth and homogeneous rough reference vs. experimental data of Nikuradse (1931) and the correlation proposed by Dean (1978) . k_s denotes the sand grain size in Nikuradse's experiments or the equivalent sand grain roughness in case of the current measurements. The ratio k_{avg}/k_s is obtained from figure 5.

in the notches, creating submerged roughness strips with $h_{\mathrm{avg}} = 0$. Thus, this configuration is named sub-merged_rgh_xδ. The experimental matrix is completed with measurements of a smooth reference aluminium plate and homogeneous sandpaper.

3   Facility & Experimental Procedure

The utilized experimental facility (see figure 2) consists of an open-circuit blower tunnel developed by Güttler (2015). It allows the measurement of small changes in skin-friction drag by evaluating the static pressure at 21 pressure taps located along both side walls of a $314\,\delta$ long channel test section with an aspect ration of 12. The test section is divided into three segments of $76\,\delta$, $119\,\delta$ and $119\,\delta$ streamwise extent, where the last segment is equipped with the surface structures specified in table 1. The pressure-drop measurements in conjunction with an orifice flow meter are used to obtain the skin-friction coefficient $C_f = \frac{2\,\tau_w}{\rho U_b^2}$, which is presented in a Nikuradse-type diagram as a function of the bulk Reynolds number $Re_b = \frac{2\,\delta_{\mathrm{avg}} U_b}{\nu}$. τ_w denotes the wall-shear stress, ρ and ν the fluid's density and kinematic viscosity, respectively, and U_b the bulk velocity. Note τ_w, can be interpreted as an effective wall-shear stress that is defined upon the streamwise pressure gradient and the averaged half-channel height δ_{avg} $\tau_w = -\frac{\partial \overline{p}}{\partial x_1}\,\delta_{\mathrm{avg}}$.

The facility allows to study $C_f(Re_b)$ in the range of $4.5 \times 10^3 < Re_b < 8.5 \times 10^4$ for fully developed turbulent channel flow. The flow in the channel can be considered as fully developed turbulent channel flow for $Re_b > 4500$ downstream of $160\,\delta$ after the test section inlet, where the measurement campaign is carried out (Güttler, 2015).

For the pressure-drop measurement, a MKS Baratron 698A unidirectional differential pressure transducer with 1333 Pa maximum range and an accuracy of 0.13 % of the reading is employed. In combination with the flow rate $\dot{V}$, measured with an orifice flow meter with in-

terchangeable orifice plates, the skin-friction coefficient C_f is deduced. The orifice's pressure drop is measured with one of two Setra 239D (125 Pa and 625 Pa full-scale) unidirectional differential pressure transducers with an accuracy of 0.07 % of the full-scale, switching automatically depending on Re_b. Changes in ambient conditions are accounted for by tracking the systems inlet and outlet temperature via PT100 thermocouples and the ambient pressure and humidity using Adafruit BMP 388 and BME 280 sensors, respectively.

4   Skin-Friction Measurement Results

The obtained C_f values of the smooth and rough reference cases are shown in figure 3. It can be seen that the smooth reference case agrees very well with the correlation proposed by Dean (1978).

The measurements of the homogeneous rough reference consisting of p60 sandpaper are shown as the green markers in figure 3. For small Reynolds numbers, a gradual increase of C_f is evident indicating a transitional rough behaviour. Above $Re_b > 3 \times 10^4$, C_f converges to a constant $C_f \approx 0.0135$, indicating fully-rough behaviour. For reference, Nikuradse's original data (Nikuradse, 1931) of his famous rough pipe experiments is included in figure 3. Note that Nikuradse used uniform sized sand grains of size k_s to fabricate the rough pipes featured in his experiments. The presently investigated sandpaper is also made of sand grains, but of varying size. Thus, the averaged height $k_{\mathrm{avg}} = h_{\mathrm{avg}} \neq k_s$. However, the ratio k_{avg}/k_s can be obtained by rescaling the roughness length scale to match the roughness function ΔU in fully-rough regime with Nikuradse's data, as done in figure 5. In this framework, k_s is interpreted as the *equivalent sand grain roughness* size. The relative roughness size normalized with the respective characteristic length (half-channel height δ_{avg} or pipe radius r) is denoted in figure 3 for the individual data sets.

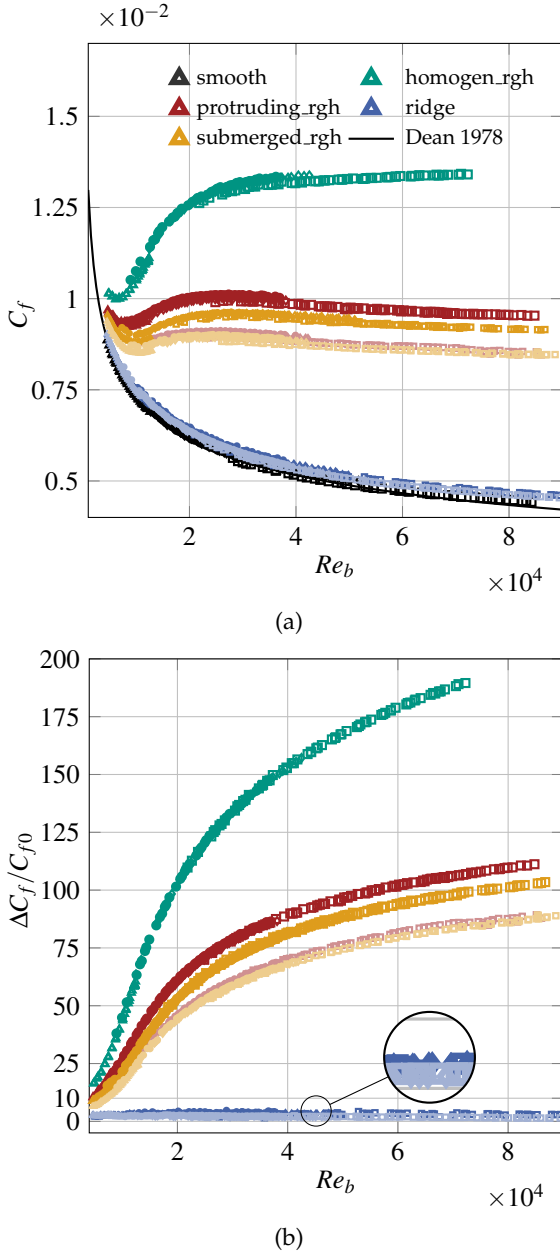Overall, the newly presented data set agrees very

(a)

(b)

Figure 4: a) Skin-friction coefficient C_f and b) relative drag increase $\Delta C_f / C_{f0}$ as a function of Re_b for investigated cases as listed in table 1. Legend of panel a) also valid for panel b). Dark color: $s \approx 2\delta_{avg}$, light color: $s \approx 4\delta_{avg}$

well with Nikuradse's measurements. For increasing r/k_s, i.e. smaller relative roughness size, the onset of the fully rough regime is shifted towards higher Reynolds numbers. The homogeneous sandpaper data set with $\delta_{avg}/k_s = 21.3$ satisfies this trend very well as it fits nicely in between the data sets with $r/k_s = 15.2$ and $r/k_s = 30.5$.

The measurement results for the inhomogeneous cases are presented in figure 4. As depicted in figure 1, three different lateral inhomogenous configurations are investigated with its dimensions specified in table 1. Individually, the two different wavelengths $s/\delta_{avg} \approx 2$ and $s/\delta_{avg} \approx 4$ were measured amounting to a total of six measurement campaigns not counting the reference

cases. The naming convention introduced in figure 1 attached with $2\delta_{avg}$ or $4\delta_{avg}$ representing the spanwise wave length are used in the following. Lighter colors represent a greater spanwise spacing.

The presence of smooth ridges only (blue datasets) of k_{avg} height produce a drag increase of 3-4 % for $s \approx 2\delta_{avg}$ and 2-3 % for $s \approx 4\delta_{avg}$.

The drag increase of the sandpaper strips exhibits a mixture of the $C_f(Re_b)$ trends of the homogeneous roughness and the smooth ridges. With increasing Re_b, $C_f(Re_b)$ decreases for all strip configurations, making it seem unlikely that a fully rough state is reached for $Re_b \to \infty$. The sandpaper strips reveal a $C_f(Re_b)$ similar (but with 40-50% more drag) to smooth ridge results (Medjnoun et al., 2020). This trend can be observed in figure 4b.

Considering the created amount of drag increase of the roughness strips, the drag increase is dominated by the presence of the sandpaper, significantly surpassing the effect of smooth ridges (by approx. one order of magnitude). Comparing the protruding (red dataset) and submerged (yellow) sandpaper configurations, the yellow submerged roughness datapoints lay below its respective protruding counterparts. Interestingly, the drag increase of the red protruding roughness datapoints exceeds the sum of the smooth (blue) ridges and submerged roughness (yellow). These observed differences in drag increase are probably related to varying strengths of the large-scale secondary motions which are expected to be strongest for the largest roughness protrusion.

From figure 4 it can be observed that all $s \approx 2\delta$ spaced configurations produce more friction drag compared to the respective 4δ configurations. From literature, it is known that the strongest secondary currents are expected for $s \approx \delta$ spanwise spacing (Vanderwel & Ganapathisubramani, 2015), recently confirmed e.g. by sPIV measurements of strip-type roughness (Wangsawijaya et al., 2020). Due to the fact that solely the wavelength s varies between cases and the surface parameters remain constant, the observed increase in friction (between $s \approx 2\delta$ and $2s \approx 4\delta$ spacing) might be an indication of stronger secondary currents in case of $s \approx 2\delta$.

5 Roughness Function

As an alternative representation to $\frac{\Delta C_f}{C_{f0}}$ discussed before, the induced drag change of surface roughness can be expressed in terms of a roughness function ΔU^+. Based on the ΔU^+ as a function of a viscous scaled roughness length scale k^+, different types of surface roughness are distinguished in literature (Jiménez, 2004). Thus, the drag-change measurements expressed as ΔU^+ are discussed in the following, as presented in figure 5.

ΔU^+ is retrieved from C_f and C_{f0} measured at the same Re_b via the following relationship

$$\Delta U^+ = \frac{1}{\kappa} \ln \frac{C_f}{C_{f0}} + \sqrt{\frac{2}{C_{f0}}} - \sqrt{\frac{2}{C_f}}, \qquad (1)$$

which is obtained from the Prandtl–von Kármán friction relation as described in Gatti et al. (2020), i.e. by approximating the change ΔU_{Cl}^+ of centreline velocity with the
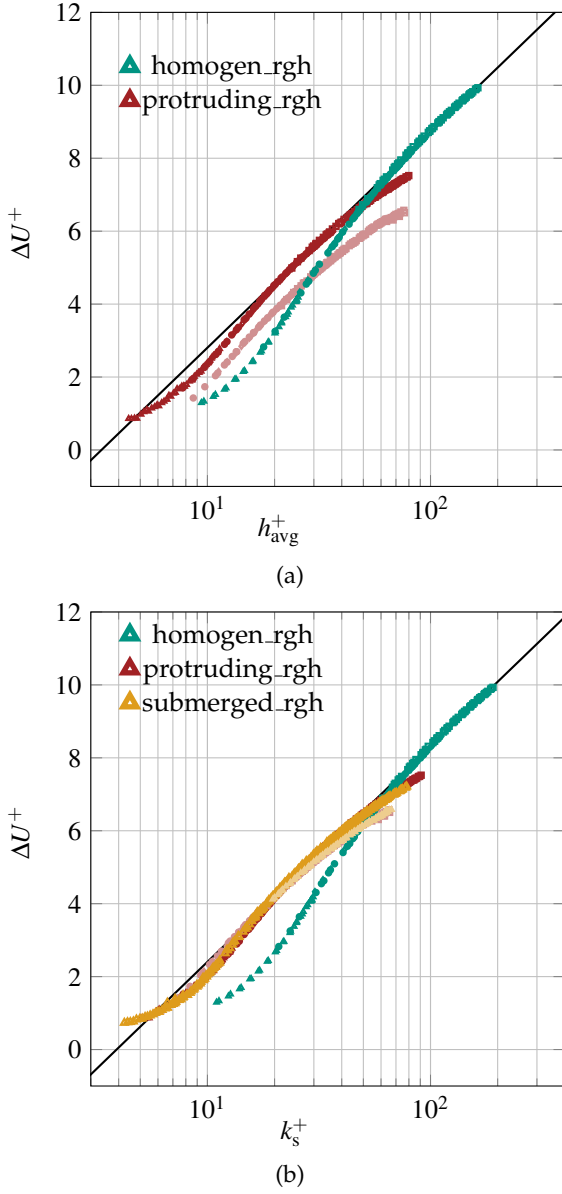
(a)

(b)

Figure 5: a) Roughness function ΔU^+ vs. h_{avg}. $\Delta U^+ = \frac{1}{\kappa} \ln h_{\mathrm{avg}}^+ + C$ with $C = -3.1$ included for reference. b) Roughness function vs. equivalent sand grain roughness k_s utilized as length scale. The fully rough reference $\Delta U^+ = \frac{1}{\kappa} \ln k_s^+ - 3.5$ is included. κ is set to $\kappa = 0.39$. dark color: $s \approx 2\delta_{\mathrm{avg}}$, light color: $s \approx 4\delta_{\mathrm{avg}}$.

change ΔU_b^+ of bulk velocity. This methodology is also employed in other studies dealing with pressure-drop measurements of flows over irregular roughness (Barros *et al.*, 2018; Flack *et al.*, 2020).

In figure 5a, ΔU^+ as a function of the domain-averaged height h_{avg}^+ is shown. Consequently, the cases submerged_rgh_$x\delta$ are not visible in this representation as $h_{\mathrm{avg}}^+ = 0$ by design. The black solid line corresponds to the fully rough behaviour (Perry *et al.*, 1969)

$$\Delta U^+(l_g^+) = \frac{1}{\kappa} \ln k^+ + B. \qquad (2)$$

with k as a roughness length scale. For choosing $k = h_{\mathrm{avg}}^+$ as in figure 5a and a von Kármán constant of $\kappa = 0.39$, an additive constant of $B = -3.1$ is obtained when matching equation (2) with the homogeneous rough reference case homogen_rgh. In this scaling, a fully-rough behaviour is evident beyond $h_{\mathrm{avg}} \approx 70$ which matches well with the reported threshold Reynolds number $Re_b = 3 \times 10^4$ as discussed before.

Comparing the case protruding_rgh_2δ to homogen_rgh and the fully-rough reference in figure 5a, a surprisingly good collapse with the fully rough regime between $20 \lesssim h_{\mathrm{avg}}^+ \lesssim 40$ is found. Beyond $h_{\mathrm{avg}}^+ \gtrsim 50$ an significantly lower ΔU^+ compared to the fully-rough reference is found. A similar departure from the fully rough regime was discussed by Gatti *et al.* (2020) in the context of purely two dimensional surface structuring aligned in streamwise direction. Bearing in mind that merely the lateral inhomogeneity is a common feature of the present study and Gatti *et al.* (2020), it is straightforward to hypothesize the absence of a fully-rough behaviour beyond a certain threshold of k^+ is caused by the surface lateral inhomogeneity.

The wider-spaced configuration protruding_rgh_4δ reveals a qualitatively very similar $\Delta U^+(h_{\mathrm{avg}}^+)$ behaviour compared to protruding_rgh_2δ in figure 5, although protruding_rgh_4δ produces less friction drag resulting in smaller ΔU^+ for matched h_{avg}^+. In order to enable a direct comparison of the sandpaper strip cases including the cases submerged_rgh_2δ with $h_{\mathrm{avg}}^+ = 0$, the equivalent sand grain roughness concept is employed. For each data set, the roughness length scale k is adjusted to match the relation for the Nikuradse sand grain roughness $\Delta U^+(k_s^+) = \frac{1}{\kappa} \ln k_s^+ - 3.5$ (Chung *et al.*, 2021). The respective ratio of the averaged roughness height k_{avg} and equivalent sand grain roughness k_s are included in table 1. Note that the homogeneous reference case homogen_rgh deviates only by 16% from the equivalent sand grain size.

The ΔU^+ results rescaled to the equivalent sand grain size k_s^+ are shown in figure 5b. In this representation, all sandpaper strip cases collapse with the fully rough reference as intended and show remarkable agreement with the fully rough regime for $15 \lesssim k_s \lesssim 30$. Interestingly, all lateral inhomogenous cases experience a clear departure from the fully rough regime supporting the hypothesis that the observed behaviour is an effect of lateral surface inhomogeneity. Moreover, the respective protruding and submerged configuration agree remarkably in the rescaled k_s representation, while the wider-spaced configurations with $s \approx 4\delta_{\mathrm{avg}}$ lead to an earlier departure from the fully rough regime.

The presented results highlight the importance to include lateral inhomogenous surface effects in predictive frameworks for ΔU^+. Significant lateral inhomogeneity leads to the absences of a fully rough regime for high Reynolds numbers. Therefore, these effects need to be accounted for based on reliable data as presented in the current study.

6 Conclusions

Overall, the presented global friction measurements add to the ongoing endeavor of characterizing & predicting flow properties of inhomogenous surfaces. Although numerous studies are available in the literature investigating inhomogenous roughness numerically and experimentally, only very few global friction measurements are available, in particular covering broad Reynolds number range. The present results provide an indication on how inhomogenous roughness effects can be embedded in engineering correlations: The amount of drag increase is dominated by the presence of roughness, while the "shape" of the $C_f(Re_b)$ bears more similarity to the the trends of smooth ridges. The presented measurements suggest that a fully rough regime is not present for roughness strips; at least not within the investigated Reynolds number range.

REFERENCES

Barros, Julio M., Schultz, Michael P. & Flack, Karen A. 2018 Measurements of skin-friction of systematically generated surface roughness. *International Journal of Heat and Fluid Flow* **72**, 1–7.

Bons, J. P., Taylor, R. P., McClain, S. T. & Rivir, R. B. 2001 The Many Faces of Turbine Surface Roughness. *Journal of Turbomachinery* **123** (4), 739–748.

Chung, D., Hutchins, N., Schultz, M. P. & Flack, K. A. 2021 Predicting the Drag of Rough Surfaces. *Annual Review of Fluid Mechanics* **53** (1), 439–471.

Chung, D., Monty, J. P. & Hutchins, N. 2018 Similarity and structure of wall turbulence with lateral wall shear stress variations. *Journal of Fluid Mechanics* **847**, 591–613.

Colombini, M. & Parker, G. 1995 Longitudinal streaks. *Journal of Fluid Mechanics* **304**, 161–183.

Dean, R. B. 1978 Reynolds Number Dependence of Skin Friction and Other Bulk Flow Variables in Two-Dimensional Rectangular Duct Flow. *Journal of Fluids Engineering* **100** (2), 215–223.

Flack, K. A., Schultz, M. P. & Barros, J. M. 2020 Skin friction measurements of systematically-varied roughness: Probing the role of roughness amplitude and skewness. *Flow, Turbulence and Combustion* **104**, 317–329.

Gatti, D., von Deyn, L. H., Forooghi, P. & Frohnapfel, B. 2020 Do riblets exhibit fully rough behaviour? *Experiments in Fluids* **61** (3), 81.

Güttler, A. 2015 High accuracy determination of skin friction differences in an air channel flow based on pressure drop measurements. https://publikationen.bibliothek.kit.edu/1000048039.

Jiménez, Javier 2004 Turbulent Flows Over Rough Walls. *Annual Review of Fluid Mechanics* **36** (1), 173–196.

Medjnoun, T., Vanderwel, C. & Ganapathisubramani, B. 2020 Effects of heterogeneous surface geometry on secondary flows in turbulent boundary layers. *Journal of Fluid Mechanics* **886**, A31.

Nikuradse, J. 1931 Strömungswiderstand in rauhen Rohren. *ZAMM - Journal of Applied Mathematics and Mechanics / Zeitschrift für Angewandte Mathematik und Mechanik* **11** (6), 409–411.

Perry, A. E., Schofield, W. H. & Joubert, P. N. 1969 Rough wall turbulent boundary layers. *Journal of Fluid Mechanics* **37**, 383–413.

Stroh, A., Schafer, K., Forooghi, P. & Frohnapfel, B. 2019 Secondary flow and heat transfer in turbulent flow over streamwise ridges p. 31.

Vanderwel, C. & Ganapathisubramani, B. 2015 Effects of spanwise spacing on large-scale secondary flows in rough-wall turbulent boundary layers. *Journal of Fluid Mechanics* **774**.

Wangsawijaya, D. D., Baidya, R., Chung, D., Marusic, I. & Hutchins, N. 2020 The effect of spanwise wavelength of surface heterogeneity on turbulent secondary flows. *Journal of Fluid Mechanics* **894**.